Electronic Supplementary Material (ESI) for Lab on a Chip.

ESI: On the acoustically induced fluid flow in particle separation systems employing standing surface acoustic waves – Part I

Sebastian Sachs, Christian Cierpka, and Jörg König
Institute of Thermodynamics and Fluid Mechanics,
Technische Universität Ilmenau, P.O. Box 100565, D-98684 Ilmenau, Germany

Mostafa Baloochi
Institute of Micro- and Nanotechnologies, Technische Universität Ilmenau, P.O. Box 100565, D-98684 Ilmenau, Germany

I. MESHING OF THE COMPUTATIONAL DOMAIN

Quadrilateral elements are used to mesh the computational domain with a width W and a height H in the numerical simulations (see Fig. S1). These elements are refined towards the boundaries by 10 to 15 layers, which thickness reduces by a factor of 1.2 with decreasing distance to the corresponding boundary. The layer closest to the wall has a thickness of 0.3δ, where δ is the thickness of the viscous boundary layer.

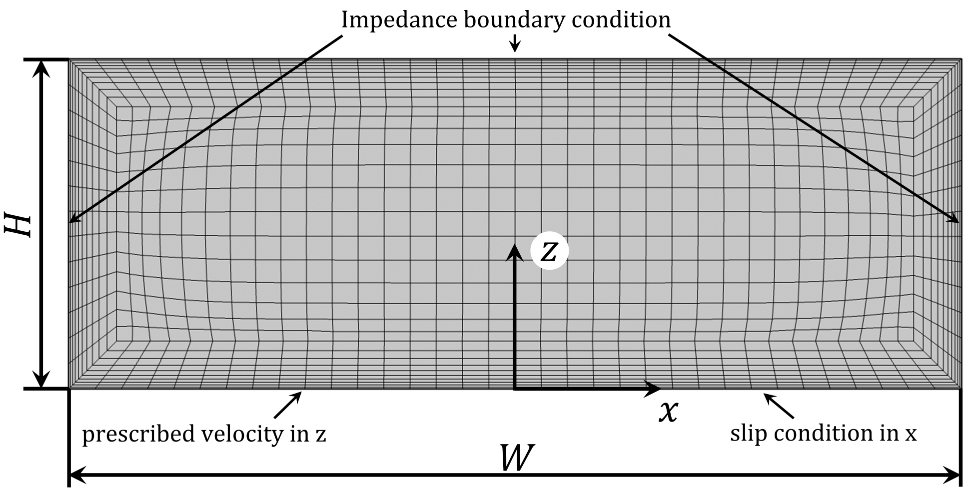

FIG. S1. Coarse meshing of the computational domain with width W and height H by quadrilateral elements. Additionally, the boundary conditions (described in section 3.2) for the calculation of the first-order fields are highlighted. For the calculation of the second-order fields the same mesh and no-slip boundary conditions were used at all channel walls.

In order to analyse the convergence of the numerical solutions with increasing number of elements, the maximum element size in the bulk $\mathrm{D_{bulk}}$ has been reduced successively. To compare the solutions g for the first and second-order fields, the relative convergence function according to equation S1 is used [1]. Here, g_{ref} represents the reference case with the smallest element size of $\mathrm{D_{bulk}} = 1\ \mu$m and a mesh with 113,050 elements. The course of C is shown in Fig. S2 as a function of $\delta/\mathrm{D_{bulk}}$. The wavelength of the SAW is constant at 90 µm and the channel height amounts to 185 µm. Considering the computational effort, a threshold for the relative convergence function was set at $C = 1.5 \times 10^{-4}$. This results in a maximum element size of 1.5 µm in the bulk, which was used for all simulations throughout this study.

$$C(g) = \sqrt{\frac{\int (g - g_{\mathrm{ref}})^2 dxdz}{\int g_{\mathrm{ref}}^2 dxdz}} \tag{S1}$$

II. PARAMETER FITTING

In order to achieve the best possible correlation between numerical and experimental results, a multilevel adaptation of several parameters was performed (see section 3.3). The results of the parameter study are summarized in Table S1. The coupling factor k_η was determined for an electrical power of 20 mW based on the minimum difference between the kinetic energy density in the experiment and simulation. For the further simulations with varying power, k_η was kept constant.

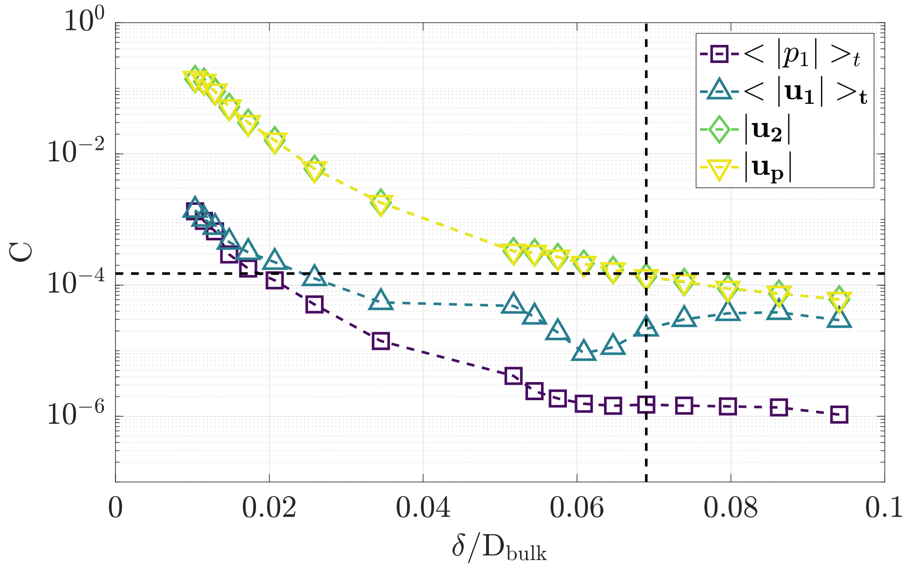

FIG. S2. Convergence function C as a function of the ratio between the viscous boundary layer thickness δ and the maximum element size in the bulk $\mathrm{D_{bulk}}$ for first and second-order quantities. The results with $\mathrm{D_{bulk}} = 1$ μm were used as reference. The horizontal dashed line indicates the threshold at $C = 1.5 \times 10^{-4}$ and the vertical dashed line denotes the corresponding element size of $\mathrm{D_{bulk}} = 1.5$ μm.

TABLE S1. Adapted parameters of the acoustic impedance of the PDMS Z_{PDMS}, slip length L_{s} and coupling factor k_η for all configurations.

Wavelength [µm]	Channel height [µm]	Impedance Z_{PDMS} [Pa s/m]	Slip length L_{s} [µm]	Coupling factor k_η
150	185	1.3×10^6	3.5	0.5782
90	185	0.9×10^6	1.5	0.4427
20	185	0.8×10^6	0.9×10^{-3}	0.0073
90	85	1.2×10^6	∞, free − slip	0.4196
90	530	1.3×10^6	∞, free − slip	0.3730

The quantitative comparison between the numerical $\boldsymbol{u}_2$ and experimental velocity fields $\boldsymbol{u}$ was realized by a normalized two-dimensional cross correlation. The algorithm is based on the following equation using the absolute time-averaged velocity fields [2].

$$R(i,j) = \frac{\sum_{x,y} \left[|\boldsymbol{u_2}(x,y)| - \langle |\boldsymbol{u_2}| \rangle_{\mathrm{A_O}} \right] \left[|\boldsymbol{u}(x-i, y-j)| - \langle |\boldsymbol{u}| \rangle_{\mathrm{A_O}} \right]}{\left[\sum_{x,y} \left[|\boldsymbol{u_2}(x,y)| - \langle |\boldsymbol{u_2}| \rangle_{\mathrm{A_O}} \right]^2 \sum_{x,y} \left[|\boldsymbol{u}(x-i, y-j)| - \langle |\boldsymbol{u}| \rangle_{\mathrm{A_O}} \right]^2 \right]^{0.5}} \tag{S2}$$

For computing the normalized cross correlation $R(i,j)$, the experimentally determined velocity field is shifted in the (x,y) plane by (i,j) relative to the numerical velocity data. Mean values of the velocity data within the overlapping area A_{O} between the two velocity fields are indicated by $\langle ... \rangle_{\mathrm{A_O}}$. The correlation coefficient $R_{\mathrm{num,exp}}$ denotes the maximum in the normalized cross correlation plane $R(i,j)$. Figure S3 shows the correlation coefficient $R_{\mathrm{num,exp}}$, plotted against the slip length L_{s} for different impedances Z_{PDMS}. Gradients in the curves reveal strong changes in the structure of the calculated velocity field, indicating a transition region between the results with no-slip ($L_{\mathrm{s}} \to 0$) and free-slip ($L_{\mathrm{s}} \to \infty$) boundary conditions. The result with the closest match to the measured particle velocity is found closer to the free-slip case. The parameter fitting results propose that a significant slip exists between the fluid and the high-frequency tangential surface deflection of the substrate.

The resulting second-order velocity fields are shown in Fig. S4 for the pure free-slip (a) and no-slip case (b). In contrast to the free-slip case, small vortex structures form in the bottom-near region with no-slip boundary conditions, which are mainly caused by the longitudinal part of the surface displacement. These are more pronounced with increasing wavelength and could not be observed in the experimentally determined velocity fields. This underlines the importance of a correct implementation of the boundary conditions at the substrate-fluid interface.

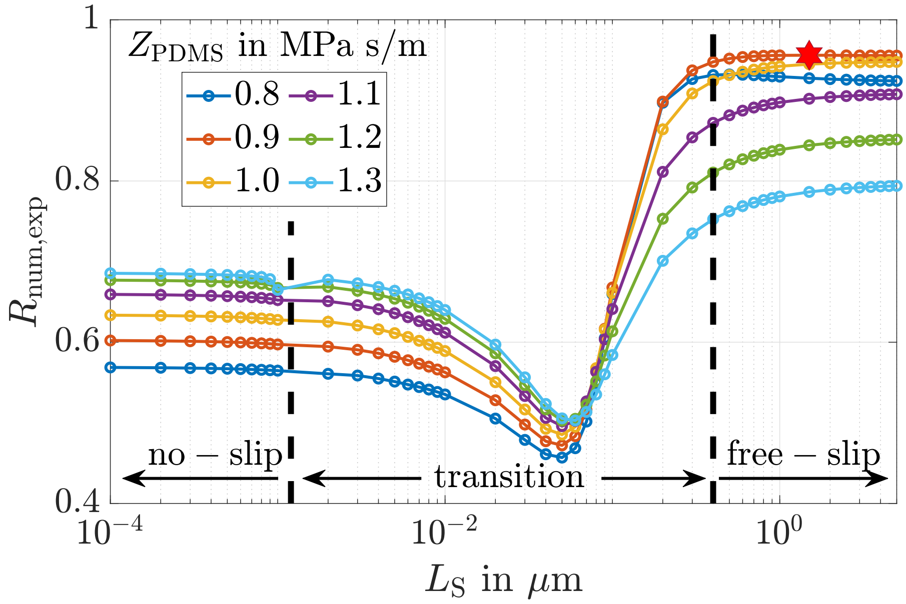

FIG. S3. Curve of the correlation coefficient $R_{\mathrm{num,exp}}$ as a function of the slip length L_s for different impedances Z_{PDMS} at a wavelength of the SAW of 90 µm and a channel height of 185 µm. Visible are areas where the numerical solution approaches the no-slip ($L_s \to 0$) or free-slip ($L_s \to \infty$) case. In between, a transition region with strong gradients in the correlation coefficient is visible. The best matching result ($Z_{\mathrm{PDMS}} = 0.9$ MPa s/m, $L_s = 1.5$ μm) is highlighted by a red hexagram.

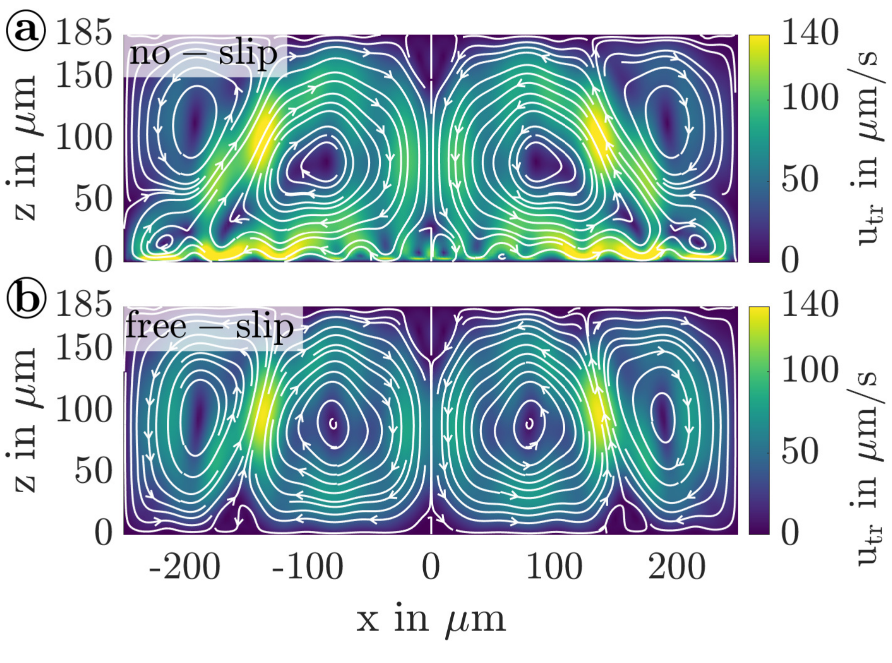

FIG. S4. Numerically determined second-order velocity fields for no-slip (a) and free-slip (b) boundary conditions on the longitudinal displacement of the substrate surface. The wavelength is constant at $\lambda_{\mathrm{SAW}} = 90$ μm.

III. TIME-AVERAGED ABSOLUTE PRESSURE FIELD

The time-averaged absolute first-order pressure field is shown in Figure S5 for different wavelengths of the SAW at a channel height of H= 185 m and an electrical power of 30 mW. As the wavelength decreases, gradients in the amplitudes become visible along both the channel width and height. Due to the specific radiation characteristics of the BAW at the Rayleigh angle, anechoic corners with significantly lower pressure amplitudes are formed in the upper corners of the channel. These are especially pronounced at a wavelength of 20 µm and provide a significant contribution to the acoustically driven flow [3, 4].

Pressure profiles along a horizontal line at $z = H/2$ reveal the periodic pattern of the pseudo standing SAW (see

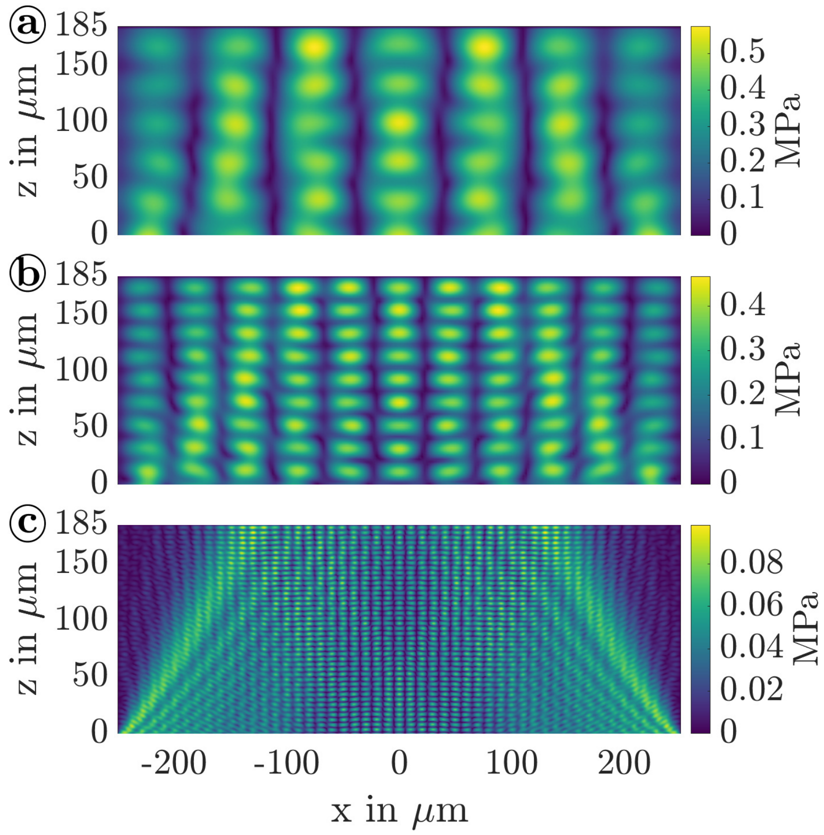

FIG. S5. Time-averaged first-order absolute pressure fields for wavelengths of 150 µm (a), 90 µm (b) and 20 µm (c) obtained by numerical simulations. The applied electrical power is constant at 30 mW in all constellations.

Fig. S6). The distances between the stationary pressure nodes in the center of the channel amount to d_{150}= 70 μm, d_{90}= 45.5 μm, and d_{20}= 10 μm and are thus close to the theoretical half-wavelength spacing of 75 µm, 45 µm and 10 µm, respectively.

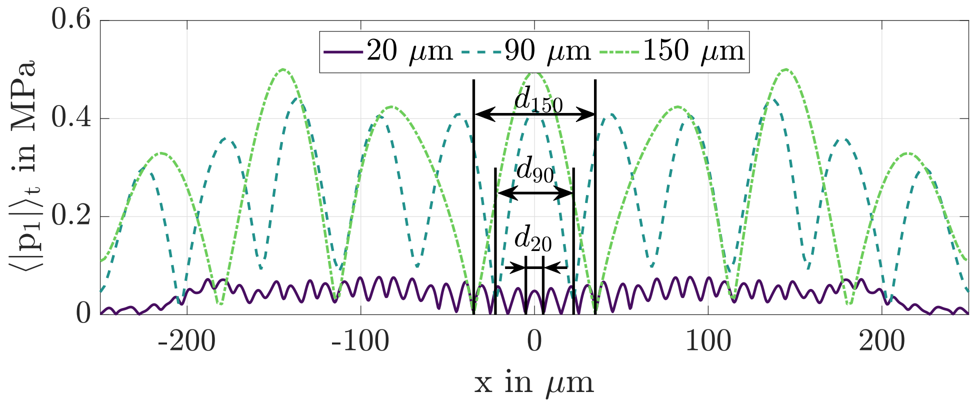

FIG. S6. Horizontal profiles of the time-averaged absolute pressure of first-order at $z = H/2$ for wavelengths of $\lambda_{\rm SAW} = 20$ μm, 90 µm and 150 µm. The corresponding distances between the pressure nodes of the standing pressure field are indicated by d_{20}, d_{90} and d_{150}.

IV. SCATTERING PARAMETER $|S_{12}|$

The scattering coefficient $|S_{12}|$ quantifies the electrical signal, that is received by one IDT after exciting a SAW at the opposite IDT. An attenuation of the SAW between the two IDTs consequently results in a lower $|S_{12}|$ value. Figure S7(a) shows $|S_{12}|$ as a function of excitation frequency for constellations without a microchannel and with a microchannel either empty or filled with fluid. It should be noted, that in this measurement the attenuation by both channel walls is included, while the SAW only passes one channel wall before reaching the fluid. If the channel is additionally filled with fluid, $|S_{12}|$ decreases further, since energy of the SAW is radiated into the fluid.

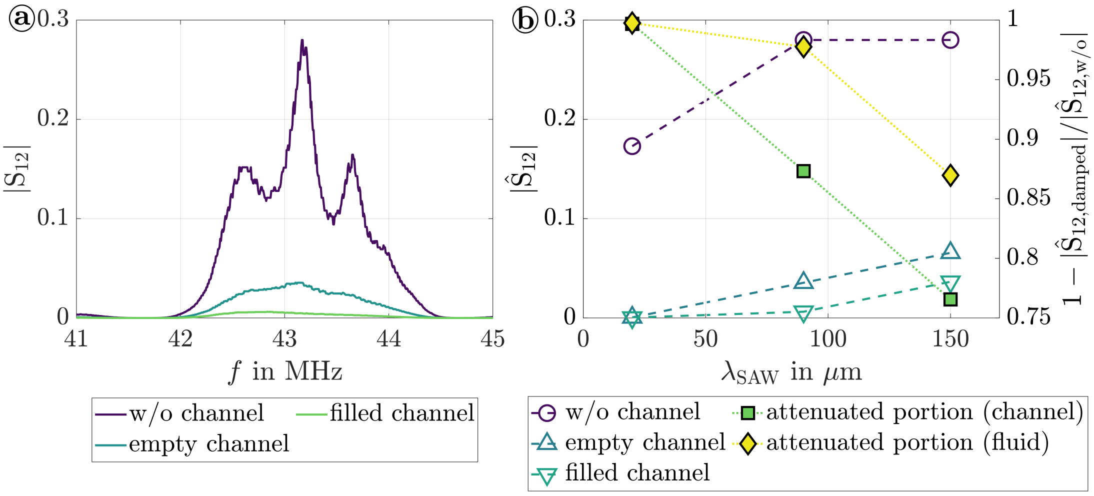

FIG. S7. (a) Curves of $|S_{12}|$ versus the excitation frequency from measurements without microchannel, with microchannel and with fluid-filled microchannel. The geometrically determined wavelength of the IDT amounts to 90 µm. (b) Amplitude $|\hat{S}_{12}|$ for different wavelengths in the constellations without microchannel, with microchannel and with additional fluid. The attenuated portions of the SAW through the channel walls and the fluid-filled channel belong to the ordinate on the right.

The amplitudes $|\hat{S}_{12}|$ are plotted in Fig. S7(b) versus the corresponding wavelength of the IDT. It can be seen that with decreasing wavelength a significantly larger attenuation already occurs through the channel walls. Based on the fraction of the signal that was attenuated by the microchannel $(1 - |\hat{S}_{12,\text{channel}}|/|\hat{S}_{12,\text{w/o}}|)$ or the fluid-filled microchannel $(1 - |\hat{S}_{12,\text{fluid}}|/|\hat{S}_{12,\text{w/o}}|)$, this development becomes even more significant. In the case of a wavelength of 20 µm and an empty microchannel attached to the substrate, $|\hat{S}_{12}|$ is reduced by 99.68 %. This proportion increases only marginally to 99.75 % when fluid is added. Compared to the measurements at larger wavelengths, the influence of the fluid decreases strongly, which indicates that proportionally less energy is radiated into the fluid due to the strong attenuation by the channel walls.

V. VELOCITY PROFILES FOR DIFFERENT CHANNEL HEIGHTS

Based on the velocity profiles of the vertical component w and w_2 along a horizontal line at $z = H/2$ in Fig. S8, two features are evident. Firstly, a significant increase of the velocity amplitude with increasing channel height is visible. Secondly, velocity fluctuations with a period close to half of the wavelength λ_{SAW} are observable for all curves. Superimposed on these fluctuations in the case of H= 185 μm as well as H= 530 μm are oscillations with a significantly longer period, which can be attributed to vortex structures extending over several pressure nodes.

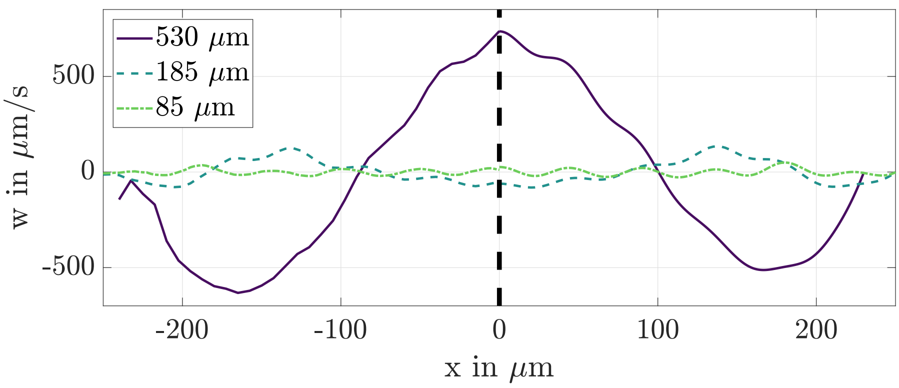

FIG. S8. Velocity profiles $w(x, z = H/2)$ or $w_2(x, z = H/2)$ for different channel heights obtained from experimental (left half) and numerical (right half) results. The supplied electric power is constant at about 30 mW.

VI. SECOND-ORDER STREAMING VELOCITY FOR OPTIMIZED CHANNEL GEOMETRIES

Figure S9 illustrates the numerical results for the second-order fluid velocity for different wavelengths. The channel cross-section was adapted in all cases according to the criteria for H_{crit} and W_{crit} in section 4.3. Periodic flow patterns are clearly visible, which were achieved throughout the wavelength range by geometry modifications. With decreasing wavelength, H_{crit} and W_{crit} also reduce, leading to a smaller channel cross-section. In a particle separation system with constant imposed volume flow rate, the fluid velocity thus increases orthogonally to the shown velocity fields. Due to the thus increasing drag force on suspended particles, the required electrical power for systems with tilted IDTs rises in order to influence particle trajectories by the acoustic radiation force.

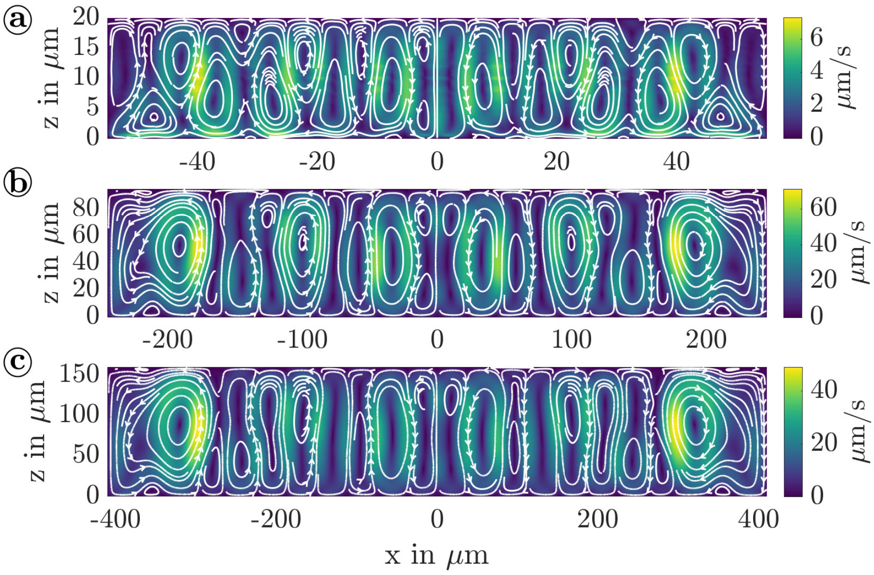

FIG. S9. Numerically calculated absolute velocity fields $u_{\mathrm{tr}} = \sqrt{u_2^2 + w_2^2}$ for wavelengths of 20 µm (a), 90 µm (b), and 150 µm (c). The fitting parameters L_{s}, Z_{PDMS}, and k_η were taken from the corresponding constellations (see section 4.3). The channel height was set to $H = 20$ μm (a), $H = 95$ μm (b) and $H = 160$ μm (c), while the channel width was specified to $W = 110$ μm (a), $W = 490$ μm (b) and $W = 820$ μm (c). Please note the different size scaling.

VII. ACOUSTIC RADIATION FORCE

The spatial distribution of the magnitude of the acoustic radiation force $|\boldsymbol{F}_{\mathrm{ARF}}|$ is depicted in Fig. S10 for a SAW wavelength of 90 µm, a channel height of 185 µm, and a particle radius of 0.69 µm. Annular structures form around the anti-nodes, while the pressure nodes organize along vertical lines between these structures. Anechoic corners are identified by lower acoustic radiation force amplitudes near the upper corners of the channel.

---

[1] P. B. Muller, R. Barnkob, M. J. H. Jensen and H. Bruus, *Lab on a Chip*, 2012, **12**, 4617–4627.
[2] J. P. Lewis, *Vision Interface*, 1995, 120–123.
[3] F. Kiebert, S. Wege, J. Massing, J. König, C. Cierpka, R. Weser and H. Schmidt, *Lab on a Chip*, 2017, **17**, 2104–2114.
[4] C. Devendran, T. Albrecht, J. Brenker, T. Alan and A. Neild, *Lab on a Chip*, 2016, **16**, 3756–3766.

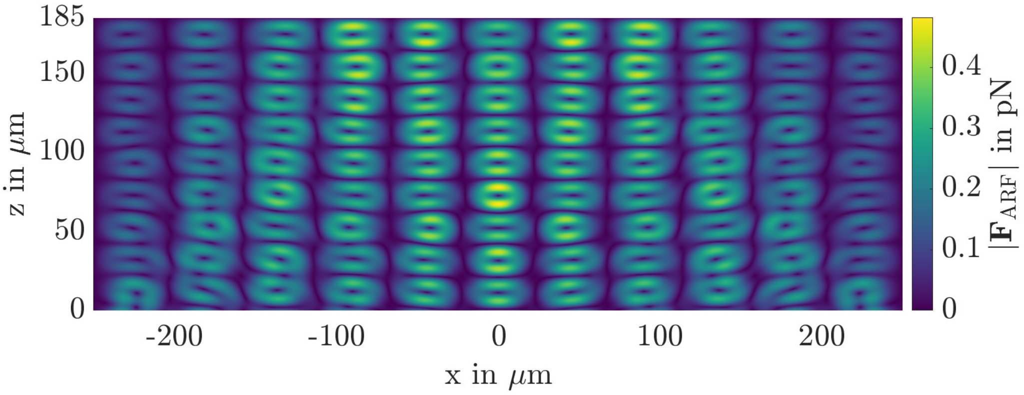

FIG. S10. Spatial distribution of the absolute acoustic radiation force over the channel cross-section for a wavelength of 90 µm, a channel height of 185 µm, an electrical power of 20 mW and polystyrene particles with a radius of 0.69 µm. The mean force coefficient amounts to $\psi \approx 1$.